Soft Matter

PAPER

View Article Online
View Journal | View Issue

Cite this: *Soft Matter*, 2024, **20**, 3806

Experimental observation of near-wall effects during the puncture of soft solids†

Christopher W. Barney, ‡[ab] Szabolcs Berezvai,[c] Allison L. Chau,[d] Younghoon Kwon,[b] Angela A. Pitenis,[d] Robert M. McMeeking,[bd] Megan T. Valentine *[b] and Matthew E. Helgeson *[a]

Received 12th September 2023,
Accepted 4th April 2024

DOI: 10.1039/d3sm01216f

rsc.li/soft-matter-journal

Performing conventional mechanical characterization techniques on soft materials can be challenging due to issues such as limited sample volumes and clamping difficulties. Deep indentation and puncture is a promising alternative as it is an information-rich measurement with the potential to be performed in a high-throughput manner. Despite its promise, the method lacks standardized protocols, and open questions remain about its possible limitations. Addressing these shortcomings is vital to ensure consistent methodology, measurements, and interpretation across samples and labs. To fill this gap, we examine the role of finite sample dimensions (and by extension, volume) on measured forces to determine the sample geometry needed to perform and unambiguously interpret puncture tests. Through measurements of puncture on a well-characterized elastomer using systematically varied sample dimensions, we show that the apparent mechanical response of a material is in fact sensitive to near-wall effects, and that additional properties, such as the sliding friction coefficient, can only be extracted in the larger dimension case where such effects are negligible.

The mechanical behavior of soft solids is critical for evaluating their suitability for use as tissue scaffolds,[1–3] drug delivery systems,[4,5] and 3D-printing inks.[6,7] Designing materials for these applications requires characterization of the elastic and failure responses to predict both how resistant a material will be to deformation and the extent of deformation at which it will fail. The elastic and failure responses of soft solids are typically quantified by a core set of conventional mechanical characterization techniques, such as uniaxial extension and notch tests.[8,9]

While conventional mechanical characterization techniques are preferred methods for evaluating materials, a growing body of literature suggests that there are instances in which a non-conventional measurement, such as deep indentation and puncture, is a more appropriate choice. For example, such instances arise when samples have a limited volume,[10] extreme reaction kinetics,[11] or brittle behavior.[12] Beyond challenging samples, conventional techniques often fall short in their ability to access high-throughput screening due to difficulty in automating the loading and unloading of samples from instrument clamps. Contact-based methods, such as indentation, currently occupy this space as a high-throughput testing method for soft solids; however, protocols often operate at low indentation depths (*i.e.*, small strains) where analysis is limited to estimates of stiffness and adhesive strength.[13,14] By contrast, in instances where the large-strain or failure response is a desired screening parameter,[15] puncture tests are a promising method for the high-throughput characterization of the non-linear behavior of soft materials.

Recent developments in the deep indentation and puncture of soft solids suggests that puncture tests are information-rich, where one test can be used to characterize the linear and nonlinear elastic, rupture, fracture, and frictional behavior of a material.[10,16–22] Puncture tests consist of inserting a needle into a material at a controlled displacement rate, while monitoring the force. After a prescribed "turnaround" displacement beyond the point of puncture, the displacement rate is reversed and the needle is retracted from the material. A typical force–displacement curve for this test (Fig. 1) shows the four stages of deep indentation and puncture,[23,24] which broadly fall into two regimes—the elastic loading and puncture regime, and the post-puncture regime. The first stage (i) includes the linear and nonlinear elastic loading of

[a] *Department of Chemical Engineering, University of California Santa Barbara, Santa Barbara, CA 93106, USA. E-mail: helgeson@ucsb.edu*
[b] *Department of Mechanical Engineering, University of California Santa Barbara, Santa Barbara, CA 93106, USA. E-mail: mtvale@ucsb.edu*
[c] *Department of Applied Mechanics, Faculty of Mechanical Engineering, Budapest University of Technology and Economics, Müegyetem rkp. 3., H-1111 Budapest, Hungary*
[d] *Materials Department, University of California Santa Barbara, Santa Barbara, CA 93106, USA*

† Electronic supplementary information (ESI) available. See DOI: https://doi.org/10.1039/d3sm01216f

‡ Current address: School of Polymer Science and Polymer Engineering, University of Akron, Akron OH, 44325, USA.

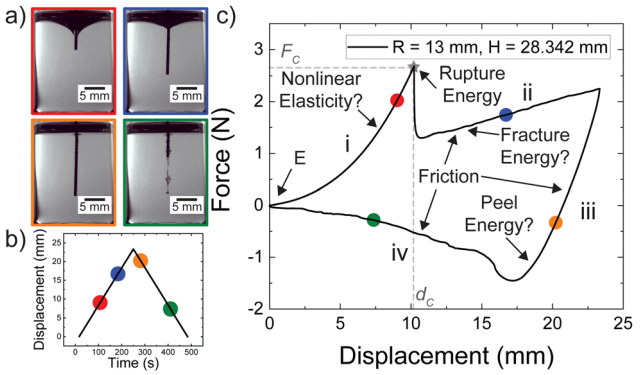

Fig. 1 (a) Images during the four stages of deep indentation and puncture from a representative run in a vial performed with a sample radius of 13 mm and height of 28.342 mm at a displacement rate of 0.1 mm s^{-1}. (b) Plot of the imposed displacement against time with the image locations marked *via* colored circles. (c) Plot of the measured force against displacement during deep indentation and puncture with the four stages of this test marked (i)–(iv). The critical puncture force F_c and displacement d_c are marked by the grey star and dashed lines. Additionally, the mechanical behavior that can be characterized during each stage has been labeled with underexplored areas denoted by question marks.

the material. The material response is described by Hertzian contact mechanics at low indentation depths while the nonlinear elastic response at large depths has been found to scale with Young's modulus E and the square of the displacement d^2.[16] This stage terminates at the critical force for puncture F_c, which is followed by an abrupt drop in the force that signals the transition to the post-puncture regime. The second stage (ii) is the "embedding stage" where the force response is dominated by friction at the walls and a steady-state crack propagation force at the needle tip. This stage terminates at the turnaround displacement of the needle. The third stage (iii) consists of retraction to reverse the shear direction at the walls and decompress the material below the needle tip. This stage terminates once the needle tip peels from the bottom of the crack generated during the embedding stage.[23] The final stage is the shear retraction stage (iv) where the forces are determined solely by the sliding friction at the needle wall. The elastic and failure responses of soft solids can be quantified by analyzing the behavior in both the elastic loading and puncture as well as the post-puncture regimes during puncture tests.

Despite the promise that puncture tests show for characterizing soft solids, particularly in a high-throughput manner, current experimental protocols do not provide quantitative advice for setting sample dimensions relative to the indenter dimensions. As a result, the volume of sample needed to perform a puncture test is ambiguous. This ambiguity allows for significant differences in both measurement and interpretation between users due to contributions in the measured force due to finite size effects – *i.e.*, the sample not being an infinite halfspace and thus being sensitive to the boundary conditions at the edges. Two major roadblocks exist for developing quantitative guidelines for setting puncture test geometries. First, numerical modeling of deep indentation and puncture is difficult due to the fine resolution of the mesh elements required to resolve large distortions that occur near the indenter tip. Treating these distortions is a substantial computational undertaking and is left to future work. The second roadblock for developing such guidelines is the lack of experiments that systematically vary the relative sample dimensions to serve as a benchmark against which future modeling can be compared.

Here, we aim to address this lack of available data by experimentally documenting how finite sample size effects influence the observed elastic and failure response of a well-characterized material during deep indentation and puncture. This is accomplished by performing deep indentation and puncture measurements on a well-characterized silicone elastomer with varied sample heights and radii relative to the indenter needle. First the materials and methods employed in this work, including those for the core puncture experiments and the additional material characterization, are presented. Then the results from the elastic loading and puncture regime as well as the post-puncture regime are presented and discussed. Finally, the limitations of this data are presented alongside a discussion of the opportunities that this work enables. These findings enable the development of quantitative guidelines for setting sample dimensions (and by extension, volume) during puncture tests and will allow puncture tests to be exploited as a high-throughput screening method.

1 Experimental

1.1 Materials

Measurements were performed on a silicone blend elastomer.[25] Samples were formed by mixing a commercially available polydimethylsiloxane (PDMS) elastomer kit, Sylgard 184, at a 30 : 1 prepolymer : curing agent ratio. This pre-cured mixture was then diluted with 100 cSt trimethylsiloxy terminated linear polydimethylsiloxane chains to a weight fraction of 0.75. The added PDMS chains (approximately 6000 g mol^{-1}) act as a non-volatile, unreactive solvent and are too short to form entanglements. Samples were mixed and then degassed under vacuum before being poured into vials and 4 inch square polystyrene Petri dishes to form samples for puncture and other additional characterization tests. All samples were cured at 70 °C for 21 hours and then immediately removed and left to cool at room temperature (22 °C) for several hours before testing.

1.2 Additional characterization

Silicone blend samples and needles were subjected to a series of characterization tests beyond the puncture measurements that form the core experiments of this work. The intent of this additional characterization was to quantify the properties that are most relevant to future modeling of deep indentation and puncture. These additional characterization methods include small strain indentation, uniaxial extension, uniaxial compression, tear tests, profilometry of the needle tip, rheometry, and sliding friction measurements. Radially confined compression has also been performed in a previous publication.[25]

Table 1 A summary of the critical properties and sample dimensions extracted from the additional characterization tests including the Young's modulus E, internal vial radius R, resilience during cyclic extension, fracture energy G_c at varied crack velocities V, average storage modulus μ' at multiple frequencies, and friction coefficient f. The bulk modulus K and Poisson's ratio ν were measured in a previous publication.[25] Full details on these methods are included in the ESI

Test	Extracted properties and dimensions				
Small strain indentation	E = 74.5 ± 15.5 kPa	R = 13 mm, R = 7.1 mm			
Uniaxial extension	E = 72.8 ± 4.9 kPa	Ogden[26] model fitting: see ESI			
Uniaxial compression	E = 73.1 ± 3.7 kPa				
Shear rheometry	$3\mu'$ = 58.1 ± 4.3 kPa	Below 10 rad s^{-1} with 0.1% strain amplitude			
Radially confined compression[25]	E = 75.3 kPa	K = 841 ± 67 MPa, ν = 0.49999 ± 0.00001			
Cyclic extension		Resilience > 94%			
Tear tests	V (mm s^{-1})	0.1	1	10	
	G_c (J m^{-2})	186.2 ± 5.9	280.8 ± 46.6	372.0 ± 19.4	
Sliding friction	V (mm s^{-1})	0.1	0.5	1	2
	f	3.16 ± 0.02	3.54 ± 0.02	3.72 ± 0.06	3.65 ± 0.05

The methods and instrumentation for each of the characterization methods used in this work are documented in the ESI.† A summary of the properties provided by these measurements is contained in Table 1.

1.3 Puncture

Deep indentation and puncture were performed on a TA.XTPlus Connect Texture Analyzer with a 50 N load cell. A 22 gauge blunt-tipped steel needle (inner and outer radius of 0.207 mm and 0.359 mm, respectively) was sourced from the Hamilton Company and mounted to the instrument using the barrel of a 3 mL luer lock tipped syringe mounted into a drill chuck fixture that connects directly to the load cell. Puncture measurements were performed in two vials with different internal dimensions. The larger vial was a 20 mL scintillation vial and had an internal radius of R = 13 mm while the smaller vial had an internal radius of R = 7.1 mm. Samples were prepared in each vial with different amounts of material to alter the sample height H. Ten different heights (3–15 mL of sample) were tested in the R = 13 mm vials and six different heights (1–5 mL of sample) were tested in the R = 7.1 mm vials. The vials of samples tested in the variable height measurements were not clamped and thus the data obtained during the retraction stage of the test are only useful up to the point where the frictional forces become equal to the weight of the sample. The majority of samples were tested with a displacement rate of 1 mm s^{-1}; however, samples with dimensions (R = 13 mm, H= 28.3 mm) and (R = 7.1 mm, H = 31.4 mm) were also tested with displacement rates of 0.1 and 10 mm s^{-1}. Four measurements with clamped vials were performed at each displacement rate. The starting height of the needle tip was recorded before measurements were performed and samples were determined not to puncture if the indenter tip reached within 100 μm of the base of the vial.

2 Elastic loading and puncture regimes

Previous work during the elastic loading regime showed that, in the absence of any near-wall effects, the relationship between F and d is well-approximated by,[16]

$$F \approx k'Ed^2 + k''Ead, \quad (1)$$

where a is the indenter radius and both k' and k'' are empirically measured constants. This established relationship assumes that the sample is sufficiently large that the boundary conditions at the edge of the sample (*i.e.*, the cylindrical vial walls) do not influence the indentation measurement. k' is typically viewed as being material-specific and reported values of this property typically span 0.25–0.5,[11,16–18] though one work has observed values on the order of 1.[10] This relationship suggests that a plot of F against Ed^2 should be linear at large d where $k'Ed^2 \gg k''Ead$ in the absence of near-wall effects to the force, as k' should be constant for a given material.

Plots showing representative curves of F against Ed^2 for the vials where (a) R = 13 mm and (b) R = 7.1 mm with varied H are contained in Fig. 2. Note that all runs from both of these plots have been individually plotted in the ESI† for additional clarity. Since a = 0.359 mm, $\frac{R}{a} = 36$ and $\frac{R}{a} = 20$ for the large and small vial, respectively. In the large vial samples, an apparent linear relationship is observed at large H while a nonlinear relationship where the sample appears to stiffen is observed at smaller H. The transition between these two behaviors appears to occur when H = 11.647 mm $\left(\frac{H}{a} = 32\right)$ indicating that finite size effects can influence measurements when the sample height is significantly larger than the indenter dimensions. Since the underlying constitutive response of the material is unlikely to change across the samples, this observed stiffening likely indicates that the measurement is being influenced by traction at the sample-vial interface. These tractions should generate some hydrostatic stress that would stiffen the apparent material response consistent with the behavior observed in Fig. 2a. In contrast to the large vials, the material response of the small vial samples (R = 7.1 mm, $\frac{R}{a} = 20$) does not appear to be significantly influenced at different sample heights. There is some nonlinearity in the two shortest samples; however, it is less pronounced than in the large vials. This appears to be counter-intuitive as one would expect radial confinement to also cause a stiffening effect. To further examine this behavior, it is useful to consider the actual values of k'.

A plot of the apparent k' values for samples calculated as $F_c/(Ed_c^2)$ (setting k'' = 0), where F_c and d_c are respectively the

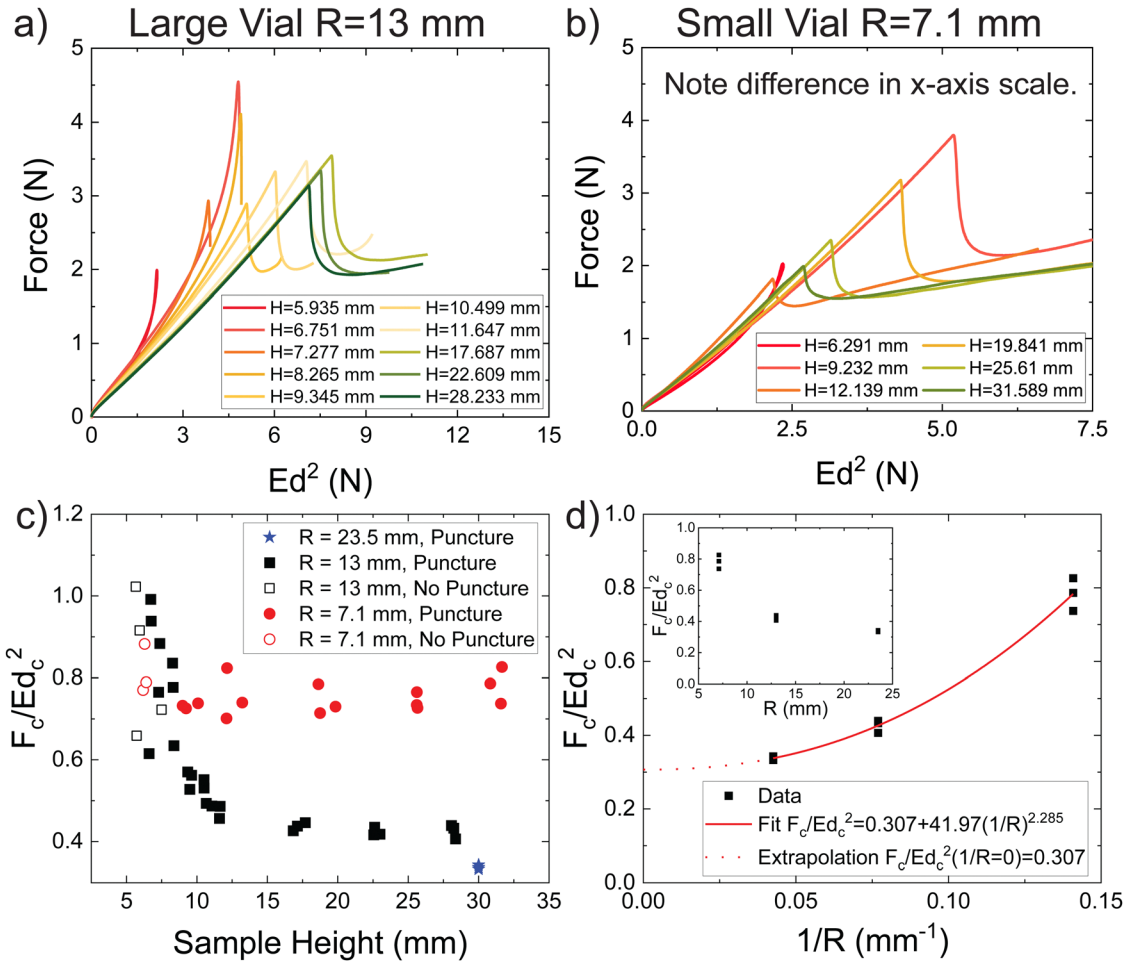

Fig. 2 Representative data plots of force against Ed^2 for vials with an internal radius of (a) 13 mm and (b) 7.1 mm. Note the difference in x-axis scale between (a) and (b). Individual plots of this data are contained in the ESI.† The impact this dimension has on the elastic loading regime is quantified with a summary plot (c) showing k' plotted against the sample height. (d) k' plotted against $\frac{1}{R}$ for the largest height samples from (c).

critical puncture force and displacement, against sample height is contained in Fig. 2c. We emphasize that these are apparent values – and not intrinsic material properties – as they are calculated in a manner that ignores finite size effects. In the large vial samples (R = 13 mm), k' has a value of approximately 0.4 at large H with a steep increase in value to a maximum of approximately 1 at small H. This trend is consistent with the full F *vs.* Ed^2 curve (Fig. 2a), indicating that deviations from the apparent k' value at large H may be a reliable indicator of the onset of finite size effects. In the small vial samples (R = 7.1 mm), the apparent k' value is largely insensitive to H and is approximately 0.75. This trend is consistent with the previous observation from the full F *vs.* Ed^2 curve, which lacks a pronounced nonlinear curvature at smaller H. Importantly, the apparent k' values for both sample vial radii do not agree at large H, with those for the small vials being almost a factor of 2 higher. This suggests that the influence of a finite sample height on the observed stiffness can be neglected if the indentation response is already dominated by the effects of the finite sample radius.

While there is a straightforward trend showing that the stiffening driven by a finite sample height is negligible when $d_c > H$, estimating the effective halfspace value of k' at large sample radius requires further analysis. To aid in this analysis, an additional data point was taken at large sample height (H = 30 mm) in 100 mL beakers that had an internal radius of 23.5 mm. A plot of the apparent k' values for the largest sample heights against $\frac{1}{R}$ is shown in Fig. 2d. Note that the inset of k' plotted against R shows an inverse dependence with R. When plotted against $\frac{1}{R}$ it is apparent that k' has a nonlinear relationship with $\frac{1}{R}$. This data was fit to a power law fit and it was found that $k' \sim \left(\frac{1}{R}\right)^{2.285\pm0.487}$. Additionally extrapolation found that the predicted halfspace value (intercept in Fig. 2d) was 0.307 ± 0.033 which is in the lower range of values often observed during puncture tests.[11,16–18] While general recommendations for managing finite size effects will require numerical modeling, this data shows that measurements of apparent k' values can be used to quantify their influence. Finite height effects are negligible when $d_c > H$ and finite radial size effects

can be quantified by extrapolating to 0 on the apparent k' *vs.* $\frac{1}{R}$ plot. Performing measurements to quantify this behavior requires a minimum of 3 samples; however, it can require more if the initial trials show that $d_c \approx H$.

Puncture of the sample occurs when a crack nucleates below the indenter and releases some of the strain energy stored in the material. The release of this energy leads to a characteristic drop in the force–displacement curve, as shown in Fig. 1. The critical puncture displacement d_c and puncture force F_c at which the crack nucleates are often used as characteristic measures of the fracture response of a material.[10,11,16] d_c and F_c are measured without notching the sample and are determined by a rupture process where the fracture energy is convoluted with the crack nucleation energy, as discussed previously.[16] In this work, and consistent with prior work,[18,20] we make the simplifying assumption that fracture energy scales with the rupture energy and thus use d_c and F_c to quantify the fracture response.

Plots of (a) d_c and (b) F_c at different sample heights are contained in Fig. 3. At sufficiently large values of H, d_c appears to be relatively constant in both vial sizes with approximate values of 10 mm and 7.5 mm in the large and small vials, respectively. The lower observed values of d_c in the small radius vials indicate the influence of a finite radial sample size. The limit where $d_c = H$ is marked in Fig. 3a by the solid line. For the larger vials, the samples appear to approach this limit when $H \approx 12$ mm, which is consistent with the onset of stiffening observed previously in the F *vs.* Ed^2 curves. This further suggests that the stiffening observed in the large vials occurs due to the indenter tip approaching the interface at the base of the vial. In the small vials, the samples appear to approach this limit when $H \approx 10$ mm, suggesting that stiffening driven by a finite sample height should not be apparent in these samples. This is consistent with the observations in Fig. 2 that suggested the small samples are mainly sensitive to the interface at the wall of the vial. Unlike d_c, F_c does not appear to have a strong dependence on the sample dimensions. As shown in Fig. 3b, F_c has significant scatter and an approximate value of 3 N in both vial sizes at all sample heights.

Similar trends and values of F_c are observed in both vial sizes regardless of the indenter velocity (*i.e.*, the strain rate) (Fig. 3c). Both samples were measured at large values of H where finite sample height effects should not influence the measurement. In the large vial, F_c decreases as the indenter velocity increases from 0.1 to 1 mm s^{-1} and then slightly increases when the indenter velocity increases to 10 mm s^{-1}. In the small vial, F_c decreases and becomes constant within the spread of the measurement at 1 and 10 mm s^{-1}. Neither of these trends are consistent with that observed in the tear tests, performed in the ESI,† where G_c was found to monotonically increase with crack velocity. This suggests that, while previous measurements have observed F_c monotonically increases with indenter velocity as G_c increases,[18] this may not be the case for all materials, geometries, and indenter velocities.

Together, the results from the elastic loading and puncture regimes suggest that the small and large vials represent two different limiting cases where finite size effects matter. In the large $\left(\frac{R}{a} = 36\right)$ vial, stiffening is driven by mechanical interactions at the interface between the sample and the base of the vial. This is consistent with the observation that, as $d_c \to H$, the measurements display both a pronounced nonlinearity in the F *vs.* Ed^2 curves and increasing apparent k' values. On the other hand, the stiff behavior of the small vial $\left(\frac{R}{a} = 20\right)$ appears to be driven primarily by mechanical interactions at the interface between the sample and the vial walls. This is consistent with the observation that d_c does not impinge upon the limit where $d_c = H$ and displays both a lack of pronounced nonlinearity in the F *vs.* Ed^2 curves as well as constant apparent k' values that are higher than those in the tall sample limit of the large vials. The consistently increased apparent stiffness in the small vials is likely due to the indenter being equidistant from the vial walls as the sample height is altered. This means that the large vial represents a case where the finite sample height primarily alters the apparent response whereas the small vial represents a case where the finite sample radius primarily alters the apparent response.

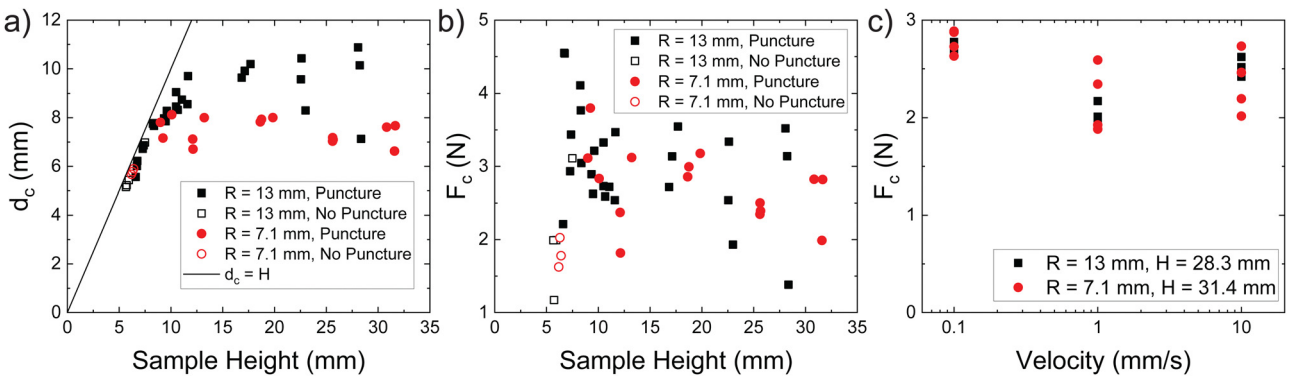

Fig. 3 Plots showing (a) d_c and (b) F_c against sample height for vials with two different internal radii. (c) Plot of F_c against velocity for samples with large sample heights.

3 Post-puncture regime

Analysis of deep indentation and puncture in the post-puncture regime is an active area of investigation.[22–24,27–29] The current understanding of crack morphology during deep indentation and puncture is that it relates to the indenter tip geometry, materials properties, distribution of materials defects, and large strain stiffening behavior.[21,30] Currently this link is qualitative and prohibits researchers from predicting the crack morphology without making measurements. The analysis used here assumes that the crack that nucleates upon puncture can be represented as an idealized planar crack and further assumes that the crack has sufficient room to reach a steady state of propagation before the turnaround displacement is reached. While these assumptions are appropriate for many samples, there are more complex crack morphologies and experimental scenarios where this analysis would not apply.[11,21,31,32] Indeed, as seen in Fig. 4a, samples that impinge upon the $d_c = H$ limit puncture close to the turnaround displacement and fail to reach steady state propagation before the indenter is retracted from the sample. Note that all runs from this plot have been individually plotted in the ESI† for additional clarity. As a result, we focus further analysis on the experiments performed using samples with large heights and only probe the influence of a finite radial size.

After puncture, the force resisting further insertion can be separated into two contributions,[22,33,34]

$$F = F_{\text{prop}} + F_{\text{slide}}, \tag{2}$$

that represent the force at the tip needed to propagate the crack F_{prop} and the sliding friction that develops at the walls of the indenter F_{slide}. Assuming that the crack propagates in a self-similar manner, F_{prop} should not vary as the displacement increases. Assuming a penny-shaped crack geometry at the indenter tip gives $F_{\text{prop}} = (\pi a)^{3/2}\sqrt{\frac{EG_c}{3}}$ when one assumes a linear elastic response for the fracture propagation.[35] F_{slide} can be determined by multiplying the critical sliding stress τ_c by the area A of contact at the needle walls.[22] A is estimated as the circumference of the needle $2\pi a$ multiplied by the contact length l which should scale directly with d. Thus the total force can be expressed as

$$F = (\pi a)^{3/2}\sqrt{\frac{EG_c}{3}} + 2\pi a l \tau_c. \tag{3}$$

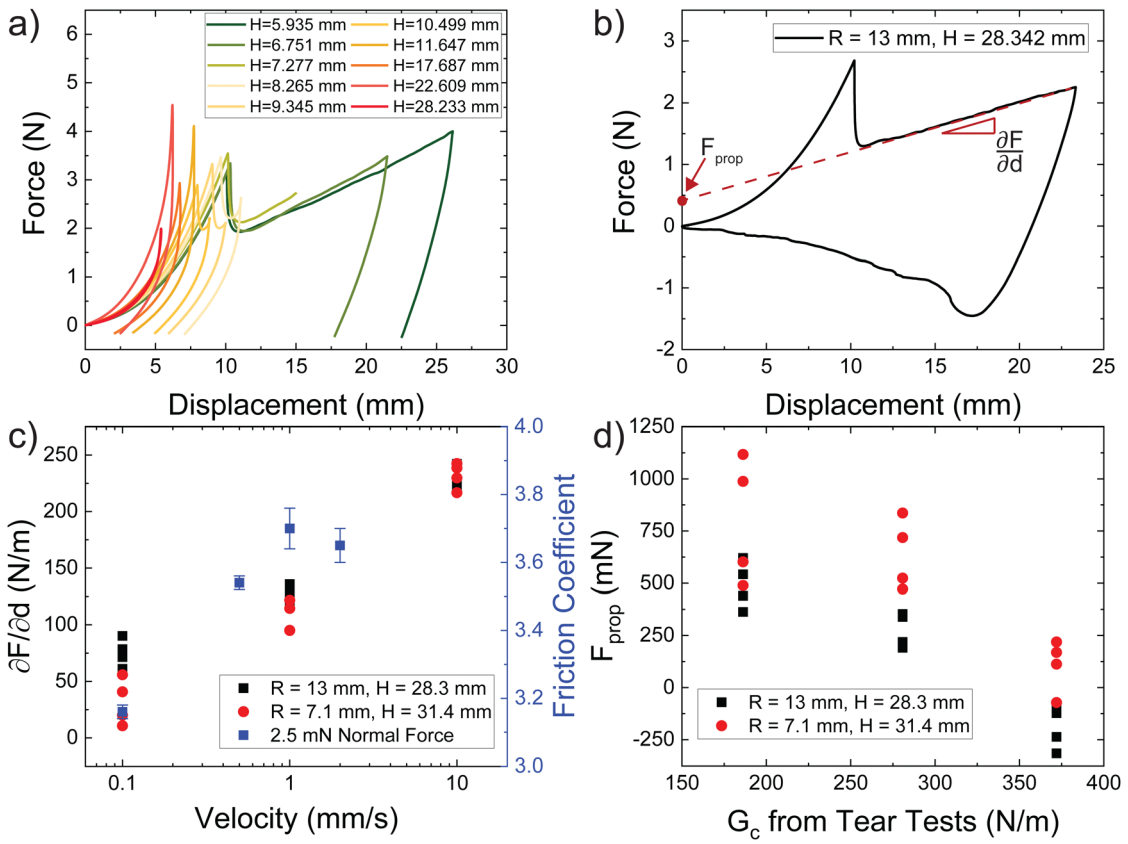

Fig. 4 (a) Raw force–displacement curves for large vial (R = 13 mm) samples that are not clamped. Individual plots of this data are shown in the ESI.† It is apparent from this data that samples approaching the $d_c = H$ limit lack the room to develop a steady state of propagation before turnaround. (b) A representative force–displacement curve for a clamped vial sample displaying the embedding slope $\frac{\partial F}{\partial d}$ and intercept propagation force estimate F_{prop}. (c) $\frac{\partial F}{\partial d}$ and friction coefficient, measured independently in the ESI,† against sliding velocity for vials with two different internal radii. (d) Plot of F_{prop} against G_c, measured independently, for samples with two different internal radii.

Here, both terms that determine F depend on velocity through the dependence of E, G_c, and τ_c on velocity.

Notably, F_{prop} does not depend on d while F_{slide} does through l. This means that the slope on the force–displacement curve $\frac{\partial F}{\partial d}$ provides characteristic information about the sliding friction. It also suggests that F_{prop} can be quantified by extrapolating to $l = 0$ where $F_{slide} = 0$, which should occur when $d = 0$. This possible treatment of the data is illustrated in Fig. 4b. $\frac{\partial F}{\partial d}$ is calculated from the embedding stage and F_{prop} is calculated by extrapolating this line to $d = 0$.

A plot of the resulting values of $\frac{\partial F}{\partial d}$ and the friction coefficient, measured as part of the additional materials characterization presented in the ESI,† against the sliding velocity is shown in Fig. 4c. These data show that both $\frac{\partial F}{\partial d}$ and the friction coefficient increase as the sliding velocity increases. This suggests that the frictional stresses increase due to an increase in the friction coefficient. The critical sliding stress is smaller in the small vials at the 0.1 and 1 mm s^{-1} sliding velocities while no difference is observed at 10 mm s^{-1}. This suggests that finite radial size effects become less important as the sliding velocity increases.

A plot of F_{prop} against G_c, measured *via* tear tests discussed in the ESI,† is contained in Fig. 4d. For all sliding velocities, F_{prop} is observed to be larger in the smaller vials. Notably, F_{prop} decreases to the point that it eventually becomes negative as G_c increases. These negative values are nonphysical as F_{prop} would then work to close the crack instead of open it so that the crack can propagate. The decreasing trend and negative values of F_{prop} at higher sliding velocities possibly indicates a diminishing and eventual loss of the ability to extract F_{prop} as the frictional component becomes too large to sense the crack tip propagation stress. Further, the observation that F_{prop} varies between vials suggests that the relative magnitudes of F_{prop} and F_{slide} are sensitive to boundary conditions. Taking the lowest sliding velocities, where the frictional stresses are lowest, the predicted magnitude of F_{prop} can be calculated by using independently measured reference values (Table 1) in the first term in eqn (3). This gives a predicted value of 82 mN, which is an order of magnitude lower than the approximate value of 500 mN found through the force–intercept method. Given that $G_c \sim F_{prop}^2$, estimating G_c from the experimentally observed F_{prop} would overestimate G_c by two orders of magnitude. This discrepancy suggests that either the method of extracting F_{prop} is flawed or the theoretical form of F_{prop}, which assumes that linear elastic fracture mechanics are valid, is incorrect.

Recently, it has been suggested that the slope in the shear retraction stage should be the negative value of that in the embedding stage.[22] Examining the force–displacement curve in Fig. 4a, it is apparent that, while the curve is fairly linear in the embedding stage, it is curved and not as smooth in the shear retraction stage. This is caused by the jagged nature of the crack that forms during puncture, and an example image of this can be seen in Fig. 1a (enlarged version in ESI†). This jaggedness results in a non-uniform contact pressure and causes jumps in the force–displacement curve due to stick-slip events that occur as the tip slides across these features. As a result, the comparison of these slopes is not performed in this work, though previous measurements have found that these slopes are roughly equal and opposite in sign.[36]

Together, these results suggest that finite radial size effects influence measurements in the post-puncture regime by increasing the apparent values of F_{prop} and decreasing the apparent values of F_{slide} in smaller vials. It was also found that characterizing sliding friction from F_{slide} is very promising while extracting G_c from F_{prop} merits additional consideration. Further it was found that examining the post-puncture mechanics was only useful in the case where $d_c \ll H$ so that a steady state crack propagation process could develop.

4 Conclusions and opportunities

This work examined the influence of finite size effects on the apparent material response during deep indentation experiments. Finite size effects were found to be important in the elastic loading and puncture as well as the post-puncture regimes. For the materials studied here, confinement effects in the loading direction are apparent when $\frac{H}{d_c} \lesssim 1$, whereas radial confinement effects are detectable up to at least $\frac{R}{a} \sim 65.5$. While the measurements presented show that deep indentation and puncture is sensitive to the influence of boundary conditions at the sample edges, there are some limitations to these findings. First, while an experimental pathway for quantifying the effect of finite size was demonstrated, general guidelines for managing them were not developed. Creating such guidelines will require numerical modeling of deep indentation and puncture which is challenging given the large distortions that occur near the indenter tip and is left to future work. Second, these results highlight the current gap in understanding of the mechanical response in the post-puncture regime. Additional measurements in a system that has a lower or tunable friction coefficient to further examine the prospect of extracting a fracture energy is of interest in the future. Together these measurements are a vital step towards implementation of deep indentation and puncture as a high-throughput screening method.

Conflicts of interest

There are no conflicts to declare.

Acknowledgements

The authors would like to thank David Bothman for help gathering the needle profilometry data. This work was supported by the Materials Research Science and Engineering Center (MRSEC) Program of the National Science Foundation under Award No. DMR 2308708 (IRG-1 and IRG-2). This work

was performed within the research facilities within the California NanoSystems Institute, supported by the University of California, Santa Barbara and the University of California, Office of the President, and leveraged resources supported by the National Science Foundation under Award No. DMR-1933487. Szabolcs Berezvai has been supported by the Hungarian National Research, Development and Innovation Office (NKFIH-PD-137806) and by Janos Bolyai Research Scholarship of the Hungarian Academy of Sciences. Allison Chau acknowledges support from the NSF Graduate Research Fellowship Program under Grant No. 1650114. Angela A. Pitenis acknowledges funding support from the NSF CAREER award (CMMI-CAREER-2048043).

References

1 S. Yang, K. Leong, Z. Du and C. Chua, *Tissue Eng.*, 2001, **7**, 679–689.
2 S. Yang, K. F. Leong, Z. Du and C. K. Chua, *Tissue Eng.*, 2002, **8**, 1–11.
3 I. M. El-Sherbiny and M. H. Yacoub, *Global Cardiol. Sci. Pract.*, 2013, **2013**, 38.
4 L. Tan and B. Tan, *Chem. Soc. Rev.*, 2017, **46**, 3322–3356.
5 M. J. Webber and R. Langer, *Chem. Soc. Rev.*, 2017, **46**, 6600–6620.
6 A. Z. Nelson, K. S. Schweizer, B. M. Rauzan, R. G. Nuzzo, J. Vermant and R. H. Ewoldt, *Curr. Opin. Solid State Mater. Sci.*, 2019, **23**, 100758.
7 X. Kuang, D. J. Roach, J. Wu, C. M. Hamel, Z. Ding, T. Wang, M. L. Dunn and H. J. Qi, *Adv. Funct. Mater.*, 2019, **29**, 1–23.
8 S. P. Danielsen, H. K. Beech, S. Wang, B. M. El-Zaatari, X. Wang, L. Sapir, T. Ouchi, Z. Wang, P. N. Johnson, Y. Hu, D. J. Lundberg, G. Stoychev, S. L. Craig, J. A. Johnson, J. A. Kalow, B. D. Olsen and M. Rubinstein, *Chem. Rev.*, 2021, **121**, 5042–5092.
9 X. Zhao, X. Chen, H. Yuk, S. Lin, X. Liu and G. Parada, *Chem. Rev.*, 2021, **121**, 4309–4372.
10 S. Rattan, L. Li, H. K. Lau, A. J. Crosby and K. L. Kiick, *Soft Matter*, 2018, **14**, 3478–3489.
11 S. J. Bailey, C. W. Barney, N. J. Sinha, S. V. Pangali, C. J. Hawker, M. E. Helgeson, M. T. Valentine and J. R. de Alaniz, *Mater. Horiz.*, 2022, **9**, 1947–1953.
12 C. W. Barney, M. T. Valentine and M. E. Helgeson, *Soft Matter*, 2022, **18**, 4897–4904.
13 Y. Chen, Q. Wang, C. E. Mills, J. G. Kann, K. R. Shull, D. Tullman-Ercek and M. Wang, *ACS Cent. Sci.*, 2021, **7**(7), 1135–1143.
14 F. Xu, B. Corbett, S. Bell, C. Zhang, M. B. Hartono, Z. J. Farsangi, J. MacGregor and T. Hoare, *Biomacromolecules*, 2020, **21**, 214–229.
15 J. D. James, J. M. Ludwick, M. L. Wheeler and M. L. Oyen, *J. Mater. Res.*, 2020, **35**, 1227–1235.
16 S. Fakhouri, S. B. Hutchens and A. J. Crosby, *Soft Matter*, 2015, **11**, 4723–4730.
17 S. Rattan and A. J. Crosby, *ACS Macro Lett.*, 2019, **8**, 492–498.
18 S. Rattan and A. J. Crosby, *Extreme Mech. Lett.*, 2018, **24**, 14–20.
19 J. N. M. Boots, D. W. te Brake, J. M. Clough, J. Tauber, J. Ruiz-Franco, T. E. Kodger and J. van der Gucht, *Phys. Rev. Mater.*, 2022, **6**, 025605.
20 S. Fregonese and M. Bacca, *J. Mech. Phys. Solids*, 2021, **154**, 104497.
21 W. C. Lin, K. J. Otim, J. L. Lenhart, P. J. Cole and K. R. Shull, *J. Mater. Res.*, 2009, **24**, 957–965.
22 S. Fregonese and M. Bacca, *Soft Matter*, 2022, **18**(36), 6882–6887.
23 C. W. Barney, Y. Zheng, S. Wu, S. Cai and A. J. Crosby, *Soft Matter*, 2019, **15**, 7390–7397.
24 C. W. Barney, C. Chen and A. J. Crosby, *Soft Matter*, 2021, **17**, 5574–5580.
25 C. W. Barney, M. E. Helgeson and M. T. Valentine, *Extreme Mech. Lett.*, 2022, **52**, 101616.
26 R. W. Ogden, *Proc. R. Soc. A*, 1972, **328**, 567–583.
27 B. Zhang and P. S. L. Anderson, *J. R. Soc., Interface*, 2022, **19**, 1–15.
28 M. Montanari, R. Brighenti, M. Terzano and A. Spagnoli, *Soft Matter*, 2023, **19**(20), 3629–3639.
29 F. Lechenault, I. Ramdane, S. Moulinet, M. Roman-Faure and M. Ciccotti, *Extreme Mech. Lett.*, 2023, **61**, 101976.
30 Y. Wei, J. Ju, C. Creton and T. Narita, *ACS Macro Lett.*, 2023, 1106–1111.
31 A. Stevenson and K. A. Malek, *Rubber Chem. Technol.*, 1994, **67**, 743–760.
32 O. A. Shergold and N. A. Fleck, *Trans. ASME*, 2005, **127**, 838–848.
33 T. T. Duncan, J. M. Sarapas, A. P. Defante, K. L. Beers and E. P. Chan, *Soft Matter*, 2020, 8826–8831.
34 J. G. Williams and Y. Patel, *Interface Focus*, 2016, **6**, 20150108.
35 S. Kundu and A. J. Crosby, *Soft Matter*, 2009, **5**, 3963.
36 S. Fakhouri, *Cavitation and Puncture for Mechanical Measurement of Soft Solids*, Doctoral Dissertation, University of Massachusetts Amherst, 2015.